Methodology for Measuring the Frequency Dependence of Multipath Channels Across the Millimeter-Wave Spectrum

**DAMLA GUVEN[1] (Member, IEEE), BENJAMIN F. JAMROZ[2], JACK CHUANG[1],
CAMILLO GENTILE[1] (Member, IEEE), ROBERT D. HORANSKY[2] (Member, IEEE),
KATE A. REMLEY[2] (Fellow, IEEE), DYLAN F. WILLIAMS[2] (Life Fellow, IEEE),
JEANNE T. QUIMBY[2] (Senior Member, IEEE), ALEC J. WEISS[2] (Member, IEEE),
AND RODNEY LEONHARDT[2]**

[1]Radio Access and Propagation Metrology Group, National Institute of Standards and Technology, Gaithersburg, MD 20899, USA

[2]RF Technology Division, National Institute of Standards and Technology, Boulder, CO 80305, USA

CORRESPONDING AUTHOR: C. GENTILE (e-mail: camillo.gentile@nist.gov)

ABSTRACT Millimeter-wave (mmWave) communications promise Gigabit/s data rates thanks to the availability of large swaths of bandwidth between 10–100 GHz. Although cellular operators prefer the lower portions of the spectrum due to popular belief that propagation there is more favorable, the measurement campaigns to confirm this – conducted by ten organizations thus far – report conflicting results. Yet it is not clear whether the conflict can be attributed to the channel itself – measured in different environments and at different center frequencies – or to the differences in the organizations' channel sounders and sounding techniques. In this paper, we propose a methodology to measure mmWave frequency dependence, using the 26.5–40 GHz band as an example. The methodology emphasizes calibration of the equipment so that the measurement results represent the channel alone (and not the channel coupled with the channel sounder). Our results confirm that free-space propagation is indeed frequency invariant – a well understood phenomena but to our knowledge reported nowhere else at mmWave to date. More interestingly, we found that specular paths – the strongest after the line-of-sight path and so pivotal to maintaining connectivity during blockage – are the least invariant compared to weaker diffracted and diffuse paths.

INDEX TERMS 5G, calibration, channel, channel sounder, channel sounding, mmWave, synthetic aperture, wideband SAGE, wideband super-resolution algorithms, wireless systems.

I. INTRODUCTION

CELLULAR providers are migrating to the millimeter-wave (mmWave) bands – in practice 10–100 GHz – where swaths of bandwidth are available, offering more options than at microwave when auctioning off spectrum. So naturally variation in propagation across the spectrum is of keen interest. Popular belief is that propagation loss at higher frequencies is greater than at lower frequencies. This stems from Friis transmission equation [1], which assumes that the aperture length of antennas is half wavelength, translating to greater pathloss at higher frequencies simply due to smaller effective antenna area, not to the channel itself. It

is well understood, however, that for fixed effective antenna area, the line-of-sight (LoS) propagation path is actually frequency invariant [2]. What remains is multipath that arises from reflection, diffraction, refraction, etc. These paths are essential for maintaining wireless connectivity when the LoS path is blocked – a condition known as NLoS – faced often at mmWave since the channel suffers from much greater penetration loss than at microwave [2], [3]. It is the frequency dependence of the multipath that is not well understood.

A significant body of work has been amassed on the frequency dependence of the channel across the mmWave bands, from ten organizations [4]–[16] over the past six

TABLE 1. Reported frequency dependence of the pathloss exponent, RMS delay spread, and RMS angle spread.

Organization	Qualcomm [4][5]	NYU [6][7]	GaTech [8]	SE U [9][10]	TUI [11]	SurreyU [12]	CEA [13]	ITU [14]	DurhamU [15]	CRC [16]
Bands (GHz)	2.9,29,61	28,73,140	30,140,300	25.5,28,37.6,39.5	6.75,30,60	26,32,39	62,83	0.8 – 70 (14 bands)	0.6 – 70 (9 bands)	2.4 –61 (7 bands)
environment condition	indoor,outdoor LoS,NLoS	indoor LoS	indoor LoS path only	indoor LoS	indoor LoS, NLoS	indoor LoS	indoor LoS	outdoor LoS,NLoS	indoor LoS,NLoS	indoor LoS,NLoS
Pathloss exponent	LoS ↔, NLoS ↑	↔	↔	↑	↔	↔	↔	↔	LoS ↔, NLoS ↑	LoS ↔, NLoS ↑
Delay spread	LoS ↑, NLoS ↓			↔	↔	↓	↓		LoS ↔, NLoS ↓	↔
Angle spread				AZ ↓, EL ↓	AZ LoS ↔, AZ NLoS ↓, EL ↓	AZ ↔	AZ ↓			AZ ↔, EL ↑

years. Most papers report the dependence of the pathloss exponent, the RMS delay spread, and the RMS angle spread in azimuth (AZ) and elevation (EL). Table 1 provides a summary of the findings for each of these channel metrics, expressed either as increasing (↑), decreasing (↓), or exhibiting no trend (↔) over frequency: The pathloss exponent in LoS / NLoS is reported to either increase or exhibit no trend, and so at least appears to not decrease; remarkably, in [6], [7] the pathloss is better at 140 GHz than at 28 GHz and at 73 GHz with directional antennas but worse with omnidirectional antennas. In LoS, the delay spread increases, decreases, or exhibits no trend, whereas in NLoS it either increases or exhibits no trend. The AZ spread either decreases or exhibits no trend while the EL spread, when reported, either increases or decreases.

It is difficult to garner a clear understanding of frequency dependence from the results that have been reported thus far, yet this is not due to lack of measurements. So either the results are accurate and the channel exhibits very complex behavior, or the results reported are specific to the channel sounders and sounding techniques used for measurement, which vary drastically between organizations. To minimize the impact of the latter in order to study the former, special care must be taken to calibrate (i.e., de-embed) the channel sounder equipment from the measurements, so the dependence reported represents the channel alone (and not the channel coupled with the channel sounder).

The conventional procedure for calibration is to disconnect the antennas from the channel sounder and to calibrate the RF front ends between the antenna ports and the antennas separately.[1] To calibrate the front ends, a full two-port calibration is prescribed for vector network analyzer (VNA)-based systems [8], [13], [16]; other correlation-based systems employ a back-to-back method [9]–[12], [15]. These calibration procedures have been well established for years and so are relatively standard and straightforward, yet some do not calibrate the front ends at all [4]–[7].

Next is calibration of the antennas. Most of the aforementioned papers sound the channel by scanning a pair of horns at the transmitter (T) and receiver (R) via mechanical rotators and recording the channel impulse response (CIR) between each scan pair – horns are the antenna of choice because their directional patterns provide high gain to compensate for the greater pathloss at mmWave. Distinct propagation paths in the CIRs are discriminated as peaks arriving with different delays. The antennas are subsequently de-embedded from the measurements by dividing the received power of the paths by the boresight antenna gains of the scan pair, to obtain path gain. The problem with this approach is that paths will arrive not only with different delays, but also at different angles; and the farther the angle from boresight, the greater the estimation error in path gain. This effect is exacerbated at narrower beamwidths since the roll-off in antenna gain is steeper with angle. Another problem with this approach is that a single path will be detected by multiple scan pairs and, even though its angle is the same over all pairs, the path will be detected with different antenna gains per scan by virtue of the rotating horns. This can be especially problematic for antennas with radiation patterns having strong back lobes, as many horns do. As such, the single path will be counted multiple times and each time with a different path gain. This effect is exacerbated at wider beamwidths since the roll-off in antenna gain is gentler with angle, so more steer pairs will detect the single path.

The two contrasting beamwidth effects described above inevitably tie the channel metrics computed to the antennas employed. To mitigate the effects, super-resolution algorithms such as CLEAN [30], SAGE [31], RiMAX [32], MUSIC [33], and ESPRIT [34] synthesize the paths detected across the scan pairs into a unique set of paths, and as a biproduct estimate the path angles so that antenna gain can properly be de-embedded based on the path's actual angle (not the pair's boresight angles). Yet, super-resolution algorithms are implemented only in [16]. And to enable precision antenna de-embedding, it is spherical angle (AZ and EL) that must be estimated, yet only a few papers do [9]–[11], [16] – the others either estimate AZ only [12], [13] or no angle at all. Finally, although an antenna may be classified as omnidirectional [15], antenna gain is never truly omnidirectional in both planes and so its effects on estimated path gain cannot be ignored.

---

1. The conventional procedure cannot be applied to all systems, e.g., with integrated phased-array antennas since the RF front ends and the antennas reside on the same printed circuit board. As such, over-the-air (OTA) calibration procedures are necessary [28], [29] – but that is not the case for any of the systems considered in this paper.

Aside from the angular dependence of antennas, because the antennas employed in the cited papers are all wideband, their gain is also frequency dependent. So to enable precision antennas de-embedding, the antenna must be characterized both as a function of spherical angle and of frequency – as is done in [16] – whereas the other cited papers simply approximate antenna gain at the center frequency of the band. Aside from calibrating the RF front ends and antennas, calibration of the RF cables is essential, yet none of these papers has considered it thus far.

In any case, when different channel sounders are deployed by different organizations to record measurements [14], a meaningful comparison across bands is difficult to obtain since specific calibration procedures will vary from organization to organization. This is true even when different channel sounders are used by the same organization [4]–[8], [15] since calibration is never perfect. The comparison is more meaningful when the same organization uses the same channel sounder across all bands, albeit with different antennas [9]–[12]. When possible, it is preferable to use both the same channel sounder and the same antennas across all bands, yet this has not been done this far. In addition, the bands evaluated should have the same widths so that the delay resolution – this is critical to super-resolution algorithms – and the noise power[2] are the same, but this is the case only for [9], [10], [12], [13]. Finally, for a controlled study of frequency dependence, the environment considered must be exactly the same across all bands, but this is not the case in [6], [7], [13].

In this paper, we propose a methodology to measure frequency dependence across the mmWave spectrum, considering the 26.5–40 GHz band as an example. Our channel sounder is VNA based, coupled with a robotic arm that traces out a virtual phased-array antenna [17]–[27]. The main advantage of the virtual array versus the mechanical rotators that the other papers employ is that the beam synthesized by the array can be electronically steered towards any direction within the antenna beamwidth in postprocessing, rendering enhanced precision in angle estimation. The three main contributions of our work are:

1. Calibration procedures to de-embed the channel sounder equipment from the measurements, namely full two-port calibration of the VNA including the effects of cabling, characterization of the antennas both in spherical angle and in frequency, and position calibration of the robotic arm (Section II);
2. An extended implementation of SAGE, which like [16] de-embeds the antennas in both spherical angle and frequency, but since ours is a single channel sounder with a single pair of antennas, extracts the *continuous* frequency dependence across the band from a single measurement, lest the disjoint analyses per band conducted in [16] for which a different number of

paths may be extracted from each. Rather, we provide the continuous frequency dependence for each path extracted (Section III);
3. Measurements in two real environments – an industrial environment and a conference room – and classification of the paths against the objects on which they were incident, as well as classification of the incidence as either a specular reflection, diffraction, or diffuse reflection, to understand the frequency dependence of each (Section IV).

The last section is reserved for conclusions.

II. SAMURAI CHANNEL SOUNDER

This section describes the NIST SAMURAI (Synthetic Aperture Measurement UnceRtainty for Angle of Incidence) channel sounder [35], [36], for recording channel measurements. The system hardware is first described, followed by procedures implemented to calibrate the system.

A. SYSTEM DESCRIPTION

A photograph of the SAMURAI channel sounder is displayed in Fig. 1. The T and R antennas are matching, vertically polarized pyramidal horns with 17 dBi boresight gain and $23°/24°$ beamwidth in AZ/EL. These are WR-28 waveguide antennas (*Eravant* SAR-1532-28-S2[3]), which have a bandpass region of $B = 26.5 - 40$ GHz, setting the bandwidth of the system to 13.5 GHz. The antennas are mounted to WR-28 waveguide fixtures which, in turn, are connected through coaxial-to-waveguide adaptors and coaxial cables to the two ports (T and R) of a VNA (*Agilent* N5245A[3]). The T horn is fixed on a tripod while the R horn is mounted on the tip of a robotic arm (*Mecademic* Meca500[3]). The T port at the VNA transmits with 0 dBm power.

The frequency response of the channel $H(f_k)$ is uniformly sampled at discrete frequencies f_k in the band by the VNA. The VNA measurements are used to determine S_{21}, the ratio of the wave going into the T antenna to the wave coming out of the R antenna as if the source and load were perfectly matched to 50 Ω. The VNA calibration accounts for imperfections in the instrument and the cables and corrects for reflections from the antennas based on S_{11} and S_{22}. The interval between the $K = 1351$ sampled frequencies f_k, $k = 1 \cdots K$ in the 13.5 GHz band is $\Delta f = 10$ MHz, corresponding to a maximum unaliased delay of $\frac{1}{\Delta f} = 100$ ns, or 30 m in path length. The bandwidth provides a delay resolution of $\Delta \tau = \frac{1}{B} = 0.07$ ns, corresponding to 2.2 cm in path length resolution. The instantaneous dynamic range per frequency sample (with no averaging) is 120 dB, as determined by the intermediate frequency (IF) bandwidth set to 100 Hz [35].

The spatial response of the channel H_{X_i} is uniformly sampled at discrete antenna positions $X_i = (x_i, y_i, z_i)$ on a synthetic aperture (a.k.a. virtual array) – hence the name SAMURAI – traced out by the robotic arm at R. The arm has

---

2. In [7], the IF bandwidth was adjusted to compensate for the different noise power of the different bandwidths.

3. Mention of product names does not imply endorsement by NIST. Other products may work as well or better.
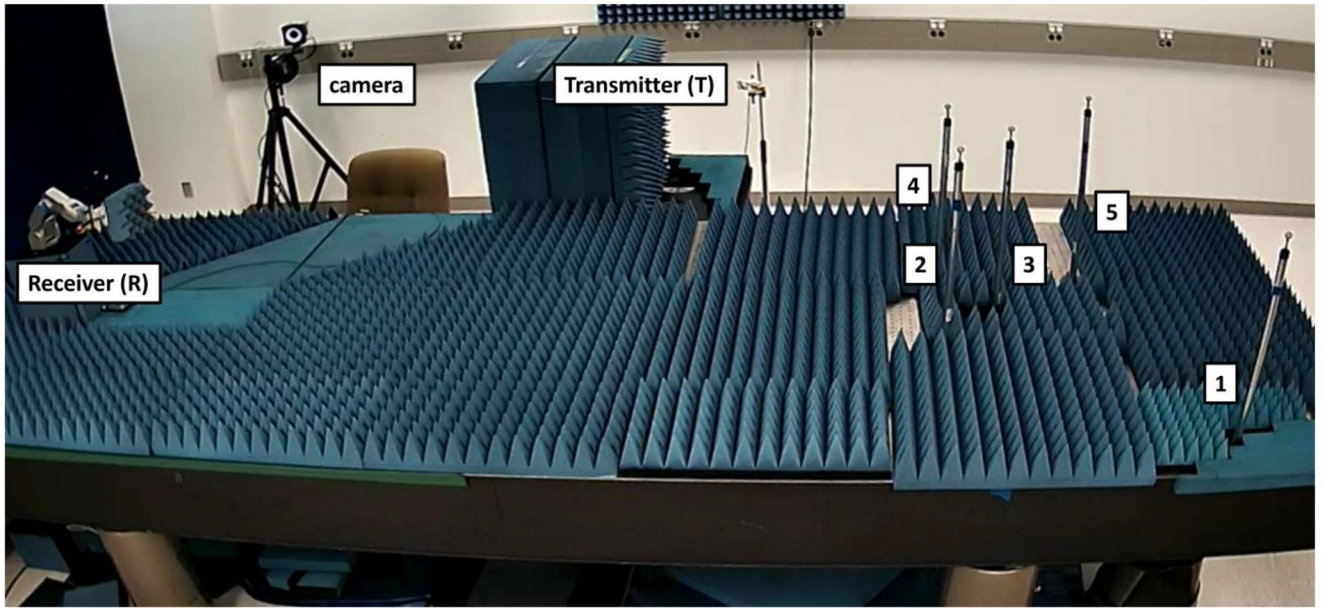
FIGURE 1. SAMURAI channel sounder in five cylinders experiment. The receiver horn antenna is mounted on a robotic arm that traces out a 35 x 35 synthetic aperture that is perpendicular to the ground, while the transmitter horn antenna is fixed on a tripod. An optical camera system estimates the aperture positions of the robotic arm to within 100 μm, and is also used to render a 3D CAD model of the environment, including ambient objects.

TABLE 2. SAMURAI channel sounder hardware.

Transmitter / Receiver Antennas
Model: *Eravant* SAR-1532-28- S2 (WR-28 waveguide horn)
Antenna gain: 17 dBi
Antenna AZ/EL beamwidth: 23°/24°
Vector Network Analyzer
Model: *Agilent* N5245A
Band, B: 26.5–40 GHz (13.5 GHz bandwidth)
Frequency interval, Δf: 10 MHz (K=1351 frequencies)
Maximum unaliased delay, $1/\Delta f$: 100 ns (30 m)
Delay resolution, $\Delta\tau = 1/B$: 0.07 ns (2.2 cm)
IF bandwidth: 100 Hz
Robotic Arm
Model: *Mecademic* Meca500
Array spacing between positions: 3.75 mm ($\lambda/2$ at 40 GHz)
Array shape: 35 x 35 (P=1225 positions) in x-z plane
Aperture length/width: 12.75 cm
Array gain: 30.9 dB
Array AZ/EL beamwidth: 3.0° (at 40 GHz)

six degrees of freedom in motion, and traces out a 35 x 35 array in the *x-z* plane perpendicular to the ground, emulating a phased array with $P = 1225$ antennas at X_i, $i = 1 \cdots P$. The frequency response is sampled at each spatial sample *i*, yielding the spatial-frequency response $H_{X_i}(f_k)$. The spacing between the antenna positions is determined by the Nyquist rate of the signal, i.e., by half the shortest wavelength λ_{MIN} in the band, which falls at $f_{MAX} = 40$ GHz. This equates to a spacing of $\frac{\lambda_{MIN}}{2} = \frac{c}{2 \cdot f_{MAX}} = 3.75$ mm, translating to an aperture length and width of $D = 12.75$ cm. The boresight of the R horn is aligned with the normal of the virtual array, set to $\boldsymbol{\theta} = (\theta^A, \theta^E) = (0°, 0°)$ as the origin of the global coordinate system. Table 2 summarizes the hardware of the SAMURAI channel sounder.

An actual phased array synthesizes an electronic beam by coherently phasing its antennas, an operation known as *beamforming*; to sample the space, the beam is scanned to different angles. A virtual array, rather, samples the space by scanning the positions on the array and beamforms to different angles in postprocessing. One advantage of virtual arrays to mechanical rotators is that the beam can be scanned towards any direction within the antenna beamwidth in postprocessing and, because virtual scanning is more precise than mechanical scanning, renders more accurate angle estimation. Another advantage is that the range of the analog-to-digital converter can be maximized since the power sampled across the virtual array will vary negligibly given the centimeters spacing between positions; in contrast, the power sampled across the beams scanned mechanically will vary widely since the same paths will be detected with different gains per scan by virtue of the highly directional beams.

A significant disadvantage of a virtual array versus an actual phased array is scan time. The time required to scan the $P = 1225$ positions is about eight hours, so only one orientation of the virtual array was examined, and the channel was kept stationary during the measurement limiting the AZ field-of-view at R to the AZ beamwidth of the horn (23°). To synthesize an omnidirectional field-of-view, as is done with most mechanical rotators, the six degrees of freedom of the robotic arm can be exploited to examine a total of eight orientations of the virtual array, each shifted by 22.5° (within the horn's AZ beamwidth) with respect to each other; this however increases the scan time to 64 hours. Nevertheless, we were able to extract many paths from the single orientation examined to substantiate the methodology proposed.

(a)

(b)

(c)

(d)
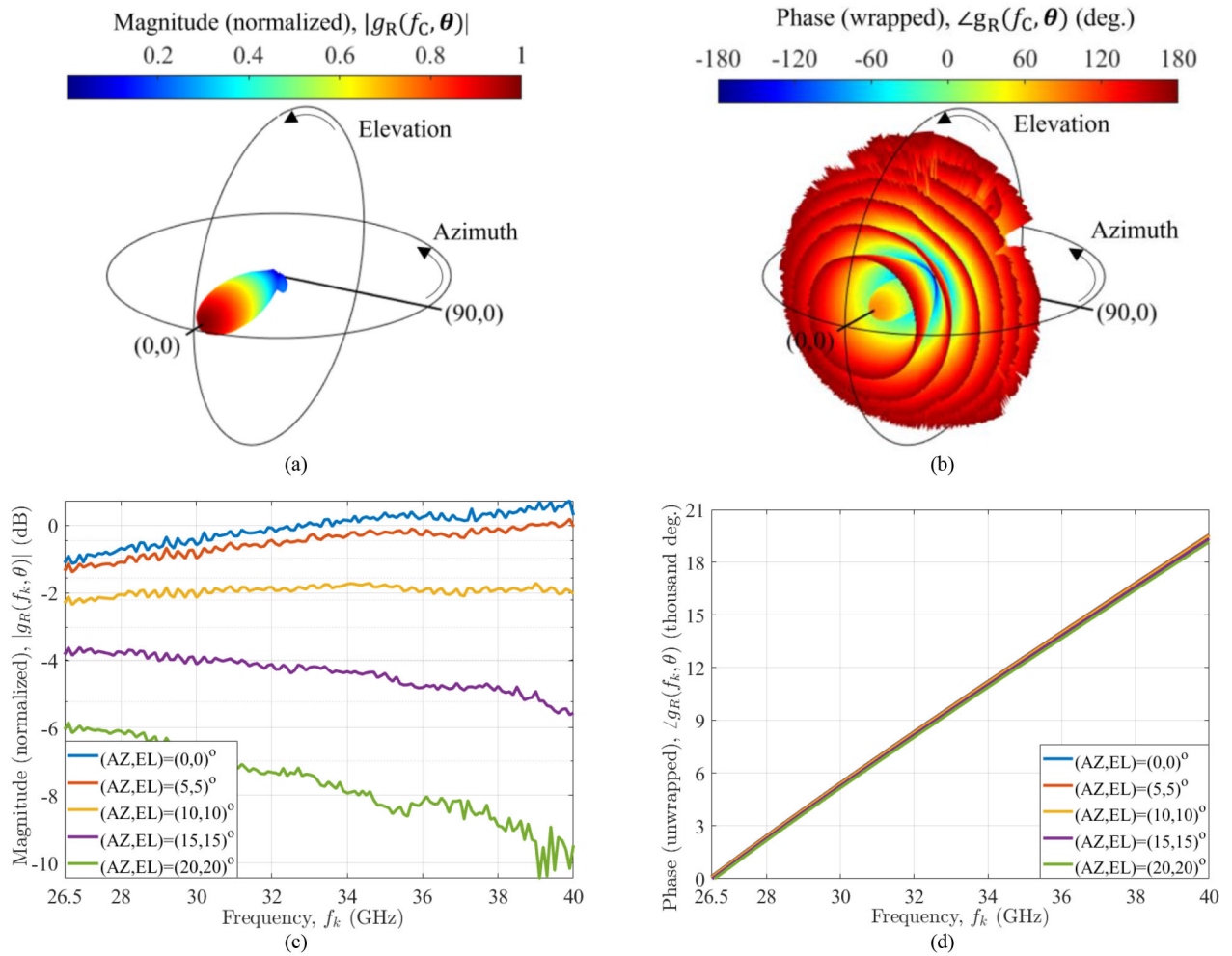
FIGURE 2. Frequency-dependent complex amplitude pattern of the R antenna, measured (a) magnitude vs. azimuth and elevation for fixed frequency (f_C = 33.25 GHz) (b) phase vs. azimuth and elevation for fixed frequency (f_C = 33.25 GHz) (c) magnitude vs. frequency for fixed elevation ($\theta^E = 0°$) (d) phase vs. frequency for fixed elevation ($\theta^E = 0°$).

B. SYSTEM CALIBRATION

Details of how the channel sounder is calibrated are provided in this section, namely calibration of the antennas, the VNA and coaxial cables, and the robotic arm.

1) ANTENNAS

The complex amplitude patterns of the T and R antennas were characterized in an anechoic chamber according to the near-field method in [37], sampled in spherical angle every 1° and in frequency every 100 MHz. As the beamwidth of the horns is only 23°/24° in AZ / EL, the characterization was conducted solely in the positive hemisphere in both planes ($-90° \leq \theta^A \leq 90°$, $-90° \leq \theta^E \leq 90°$). Fig. 2 shows the magnitude and phase patterns of the R antenna over spherical angle and over frequency.

Once characterized, the antennas were de-embedded from the measurements as part of the SAGE super-resolution algorithm, described in the next section. The antennas were interpolated down from the 1° spherical grid to continuous angle $\boldsymbol{\theta} = (\theta^A, \theta^E)$ through the technique described

in [38]. Continuous interpolation in angle – justified by the smooth roll off in magnitude and the linear phase[4] evident in Fig. 2(a) and (b) respectively – allows for any angle incident on the antennas to be precisely de-embedded. The antennas patterns were also interpolated down from 100 MHz to $\Delta f = 10$ MHz to align with the frequency response sampled by the VNA, ultimately yielding complex amplitude patterns $g_T(f_k, \boldsymbol{\theta})$ and $g_R(f_k, \boldsymbol{\theta})$. The smooth magnitude roll-off and linear phase over frequency as well, evident in Fig. 2(c) and (d) respectively, justifies the frequency interpolation.

2) VNA AND COAXIAL CABLES

The VNA was calibrated before each measurement to compensate for any frequency dependence and reflections of the measured S_{21} parameter in the measurement setup. The calibration procedure effectively normalizes the S_{21} parameter at the measurement reference planes at the input ports of the antennas to unity across the $K = 1351$ frequencies in the

---

4. The apparent discontinuities in phase in Fig. 2(b) are due to phase wrapping.

band. It was realized by disconnecting the T and R antennas from the WR-28 waveguide fixtures and connecting the fixtures to a series of Short, Open, Load, and Thru (SOLT) standards, whose electrical properties have already been well characterized as part of the calibration kit.

The coaxial cable on the R branch moves and flexes as the robotic arm translates the antenna through the $P = 1225$ positions in the 2D aperture. Through precision uncertainty analysis [39], cable bending was determined to introduce a maximum phase error of 2° (at 40 GHz) in the measurements.

3) ROBOTIC ARM

The robotic arm has a manufacturer-specified positional error within 0.1 mm. While sufficient for industrial applications – for which it was designed – the positional error is equivalent to 4.8° in phase error in our application, given that the wavelength at 40 GHz is 7.5 mm. As such, an optical camera is employed to record the actual positions traced out by the arm on the 35 x 35 grid. The camera utilizes a suite of ten cameras, each with 51° field-of-view, mounted along the periphery of the measurement environment to take snapshots at 180 frames per second of an optical marker placed on the robot tip. The camera system is pictured in Fig. 1. Once calibrated, the camera system synchronizes the multiple snapshots and triangulates the position of the robot tip to within a positional error of 0.01 mm, thus reducing the uncertainty by a factor of 10. The positions of the robot tip triangulated by the camera system are used in X_i for beamforming, as described in the next section.

III. EXTRACTION OF CHANNEL PATHS

In this section, we propose a wideband version of SAGE so that the frequency dependence of the channel paths, in addition to their narrowband properties (complex amplitude, delay, angle) for which it was designed, can also be extracted.

A. WIDEBAND BEAMFORMING

Given the architecture of the SAMURAI channel sounder, the properties of the channel paths that can be estimated are complex amplitude α and delay τ – by virtue of the VNA – and spherical angle-of-arrival (AoA) $\boldsymbol{\theta} = (\theta^A, \theta^E)$ – by virtue of the 2D array at R. (Estimation of spherical angle-of-departure (AoD) would require a 2D array at T as well.) To extract these properties, the spatial-frequency response $H_{X_i}(f_k)$ is transformed from the (X_i, f_k) domain to the $(\tau, \boldsymbol{\theta})$ domain.

First, it is transformed from X_i to $\boldsymbol{\theta}$ (for fixed f_k) through the beamforming operation, yielding the angle-frequency response:

$$H(f_k, \boldsymbol{\theta}) = \frac{1}{\sqrt{P}} \sum_{i=1}^{P} w_{X_i} \cdot H_{X_i}(f_k) \cdot S_{X_i}(f_k, \boldsymbol{\theta}), \quad (1)$$

where

$$S_{X_i}(f_k, \boldsymbol{\theta}) = e^{\frac{j2\pi f_k}{c}\left(\cos\theta^A\cos\theta^E \cdot x_i + \sin\theta^A\cos\theta^E \cdot y_i + \sin\theta^E \cdot z_i\right)}$$

is the virtual array's steering vector [40] and c is the speed of light. Beamforming synthesizes a steerable beam by coherently phasing the spatial response of the array through the steering vector, steering the beam towards $\boldsymbol{\theta}$. The half-power beamwidth of the synthesized beam varies over frequency, from 5.1° at 26.5 GHz to 3.0° at 40 GHz, in both AZ and EL since the array is square. Synthesizing the spatial response across the virtual array adds an array gain of $10 \cdot \log_{10}(1225) = 30.9$ dB to the link budget. Given the T power, the antenna gains and array gain, the instantaneous dynamic range of the system, and the 16 dB noise figure of the VNA, the maximum measurable path loss of the system is 263 dB [41].

A Kaiser taper window w_{X_i} with parameter value $\beta = 3.4$ was applied to (1) to suppress the beam sidelobes from 13.2 dB to 28.7 dB at the expense of slightly widening the main lobe from 3.0° to 3.2° (at 40 GHz); the Kaiser window was selected because it minimizes the energy in the sidelobes [42]. The beamforming operation is termed wideband because the steering vector is specific to every frequency f_k in the band, in contrast to narrowband for which f_k is replaced with the (constant) center frequency $f_C = 33.25$ GHz. As a rule of thumb, the narrowband assumption is valid when the bandwidth is less than 10% of the center frequency, for which the band is considered frequency flat [43]. In our application, B is about 40% of the center frequency, therefore wideband beamforming is necessary.

Next, the angle-frequency response in (1) is synthesized across all frequencies through the Inverse Discrete Fourier Transform (IDFT), yielding the angle-delay response:

$$h(\tau, \boldsymbol{\theta}) = \frac{1}{\sqrt{K}} \sum_{f_k \in B} w(f_k) \cdot H(f_k, \boldsymbol{\theta}) \cdot e^{j2\pi f_k \tau}, \quad (2)$$

where $w(f_k)$ is the same Kaiser taper window ($\beta = 3.4$) used in (1).

B. PATH EXTRACTION

A discrete number of paths indexed $\ell = 1 \ldots L$ is extracted from the recorded angle-delay response in (2). This is implemented in SAGE by modeling the response as a train of impulses $\delta_\ell(\tau, \boldsymbol{\theta})$, each representing a plane wave impinging on the array with delay τ_ℓ at angle $\boldsymbol{\theta}_\ell$ scaled by the complex amplitude α_ℓ, plus noise $n(\tau)$:

$$h(\tau, \boldsymbol{\theta}) \approx \sum_{\ell=1}^{L} \alpha_\ell \cdot \delta_\ell(\tau, \boldsymbol{\theta}) + n(\tau). \quad (3)$$

The impulse response of the system $\delta_\ell(\tau, \boldsymbol{\theta})$ is computed from (2) after substituting into (1) the spatial-frequency response of the system $H_{X_i}(f_k)$ to an ideal plane wave [19], or:

$$\delta_\ell(\tau, \boldsymbol{\theta}) = h(\tau, \boldsymbol{\theta}) \mid H_{X_i}(f_k) = g_T(f_k, \boldsymbol{\theta}_\ell) \cdot g_R(f_k, \boldsymbol{\theta}_\ell)$$
$$\cdot e^{-j2\pi f_k \tau_\ell} \cdot S^*_{X_i}(f_k, \boldsymbol{\theta}_\ell), \quad (4)$$
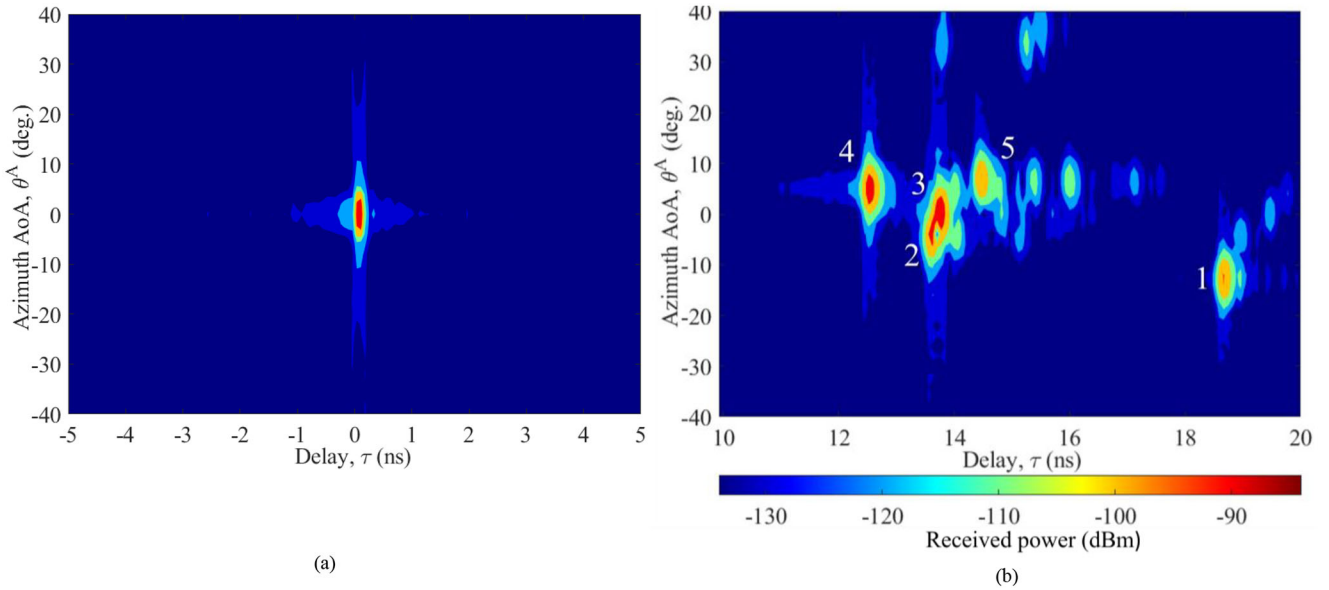
FIGURE 3. (a) Impulse response of the system $\delta(\tau, \theta)$ with the elevation AoA fixed at $\theta^{E} = 0°$. (b) Recorded angle-delay response $h(\tau, \theta)$ of the system for the five cylinders experiment with the elevation AoA fixed at $\theta^{E} = 0°$.

where $*$ denotes the complex conjugate. The impulse response is essentially a bandlimited (by B) *sinc* pulse in the delay domain centered at τ_{ℓ}. Analogously, the pulse in the AZ and EL domains is centered at $\boldsymbol{\theta}_{\ell}$ and is a function of the steering vector (and so is more complex than the *sinc* pulse). The impulse response of the system also incorporates the frequency-dependent complex amplitudes of the T antenna,[5] $g_{T}(f_k, \boldsymbol{\theta}_{\ell})$, and R antenna, $g_{R}(f_k, \boldsymbol{\theta}_{\ell})$.

Fig. 3(a) displays the impulse response of the system and Fig. 3(b) the recorded angle-delay response for the five cylinders experiment shown in Fig. 1. This controlled experiment highlights that the recorded response is just the response of the channel – the five paths – convolved with the impulse response of the system, following directly from (3). Accordingly, the path properties are extracted by deconvolving the impulse response from the recorded response. The deconvolution is executed through the SAGE super-resolution algorithm, appropriately named because it can provide delay and angle resolution beyond the inherent bandwidth and beamwidth of the system, respectively. Basically, the algorithm scales (by α_1) and translates (by τ_1 and $\boldsymbol{\theta}_1$) the impulse response to match the strongest path $\ell = 1$ in the recorded response. The scaled, translated impulse response is then subtracted from the recorded response. The process iterates L times until what remains in the recorded response is just noise, yielding L paths and their estimated properties $(\alpha_{\ell}, \tau_{\ell}, \boldsymbol{\theta}_{\ell})$, $\ell = 1 \cdots L$. In practice, we use a signal-to-noise ratio of 10 dB to avoid false detections.

---

5. As explained in Section IV.A.2, the AoD (from T) of path ℓ can be inferred directly from its combined delay τ_{ℓ} and AoA $\boldsymbol{\theta}_{\ell}$. As such, we express the T antenna gain pattern as a function of $\boldsymbol{\theta}_{\ell}$ for notational simplicity.

C. FREQUENCY-DEPENDENT COMPLEX AMPLITUDE
The delay and AoA of the paths are frequency independent since they are strictly geometrical properties, leaving complex amplitude as the only path property that can be frequency dependent. To analyze complex amplitude as a function of frequency, we consider sub-bands centered at f_k, by sliding a 2 GHz window across B at $\Delta f = 10$ MHz increments, and run SAGE on each sub-band k to extract the complex amplitude of the sub-band, denoted by $\alpha_{\ell}(f_k)$. The narrowband assumption implicit to (3) is that the complex amplitude α_{ℓ} across the sub-band is frequency flat (constant); so the sub-band cannot be too wide, yet it must be wide enough to resolve different paths. We found through trial-and-error that a value of 2 GHz achieves a good balance between the two, for which the narrowband assumption is still valid (2 GHz/f_C = 33.25 GHz $\approx$ 6%).

To analyze the complex amplitude of distinct paths across the different sub-bands, the same paths must be detected in each sub-band. This is accomplished by running SAGE on the whole band B – for which the delay resolution is finest – to extract $(\tau_{\ell}, \boldsymbol{\theta}_{\ell})$ of the L paths, in a first step. SAGE is subsequently run per sub-band in a second step to estimate $\alpha_{\ell}(f_k)$, given $(\tau_{\ell}, \boldsymbol{\theta}_{\ell})$ from the first step. The caveat is the narrowband assumption of constant α_{ℓ} across B implicit to the first step – an invalid assumption given the 13.5 GHz bandwidth – which in turn compromises the estimates of $(\tau_{\ell}, \boldsymbol{\theta}_{\ell})$. The assumption is relaxed by factoring the complex amplitudes estimated in the second step as $\alpha_{\ell}(f_k) = \alpha_{\ell} \cdot \gamma_{\ell}(f_k)$, $\gamma_{\ell}(f_C) = 1$, introducing parameter $\gamma_{\ell}(f_k)$ to explicitly model frequency dependence. The parameter is integrated into SAGE by modifying the impulse response of the system in (4) as:

$$\hat{\delta}_{\ell}(\tau, \boldsymbol{\theta}) = h(\tau, \boldsymbol{\theta}) \mid H_{X_i}(f_k) = \gamma_{\ell}(f_k) \cdot g_T(f_k, \boldsymbol{\theta}_{\ell})$$
$$\cdot \, g_R(f_k, \boldsymbol{\theta}_{\ell}) \cdot e^{-j2\pi f_k \tau_{\ell}} \cdot S^{*}_{X_i}(f_k, \boldsymbol{\theta}_{\ell}). \quad (5)$$
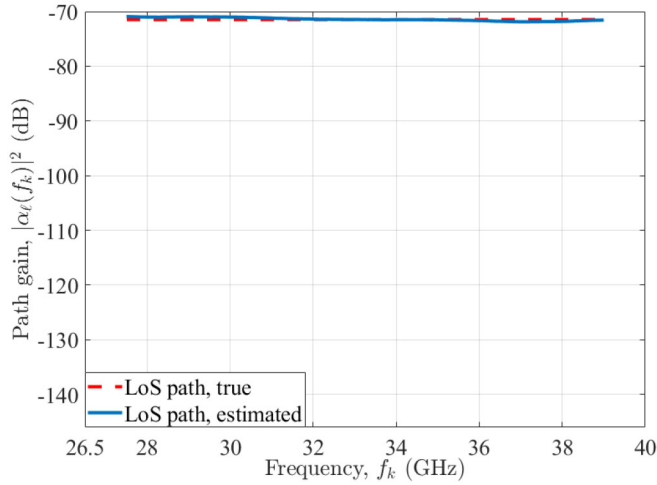
FIGURE 4. Frequency dependence of the LoS path.

FIGURE 5. CAD model of five cylinders experiment, bird's-eye view.

TABLE 3. True and estimated geometrical properties of the five cylinders.

Cylinder	Delay True Estimated (ns)	AoA AZ / EL True Estimated (deg.)	AoD AZ / EL True Estimated (deg.)
1	18.5 18.6	-11.9 / 0.0 -12.8 / -0.2	-10.9 / 0.0 -11.3 / -0.7
2	13.4 13.5	-4.0 / 0.0 -5.2 / -0.5	0.1 / 0.0 -1.1 / -0.8
3	13.6 13.7	0.1 / 0.0 0.4 / -0.4	-7.4 / 0.0 -11.9 / -0.3
4	12.3 12.5	4.4 / 0.0 4.8 / -0.4	-5.8 / 0.0 -10.7 / -0.9
5	14.2 14.4	6.0 / 0.0 7.0 / 0.1	-22.2 / 0.0 -28.0 / 0.2

Now given the modified impulse response, $\gamma_\ell(f_k) = 1$ is initialized in the first step. Then, $\gamma_\ell(f_k)$ is refined from $\alpha_\ell(f_k)$ estimated in the second step. The first and second steps are iterated until convergence.

IV. ANALYSIS OF FREQUENCY DEPENDENCE

In this section, the frequency dependence of paths extracted from the measurements is analyzed. The analysis is broken down into two parts: first, measurements were taken in two controlled environments to validate the proposed measurement methodology, by comparing estimated path properties against their ground-truth values; second, measurements were taken in two real environments to report the frequency dependence of objects that generated multipath.

A. CONTROLLED ENVIRONMENTS
1) LOS PATH

The purpose of this experiment is to confirm that the estimated frequency dependence of the extracted paths, expressed as frequency-dependent path gain $|\alpha_\ell(f_k)|^2$, is reliable. To that end, we estimated the dependence of the LoS path, which is known theoretically to have a flat response. The experiment was conducted on the optical table with the T and R horns facing each other while the surrounding objects were covered with RF absorber so that only the LoS path was detected. Fig. 4 shows that the estimated dependence (blue) matches up very well with the true dependence (red dash), deviating less than 0.5 dB across the whole band.

2) FIVE CYLINDERS

The purpose of this experiment is to confirm that the estimated geometrical properties – delay, AoA, and AoD – of the extracted paths are reliable. To that end, we placed five metal cylinders with diameter 2.5 cm on the optical table. A photograph of the setup is shown in Fig. 1 and a 2D CAD model (bird's-eye view) of the setup in Fig. 5(a), with the locations of the cylinders reported by the camera system.

Note that while the measurement system can only estimate delay and AoA, AoD can be inferred for paths with single incidence by virtue of geometrical redundancy. Specifically, delay and AoA together with known T and R locations map to a unique point of incidence, which can be traced back to T, providing AoD [45].

Table 3 shows that the true and estimated properties match up very well, with errors in delay and AoA within 0.1 ns and 1.2°, on par with the respective bandwidth and beamwidth resolution of the system. The maximum AoD error was higher – 5.8° in AZ – which can be attributed to the cumulative errors in delay, AZ AoA, and EL AoA when mapping them to AZ AoD and EL AoD.

B. REAL ENVIRONMENTS

We now turn to real environments to report the properties of the paths extracted there. Those two real environments are a Central Utility Plant – an industrial environment – and a conference room, both located on the NIST campus in Boulder, Colorado.

1) CENTRAL UTILITY PLANT (CUP)

A photograph of the measurement setup in the CUP is shown in Fig. 6(a), in which T and R were pointed towards a control panel. A total of 14 paths were extracted from the
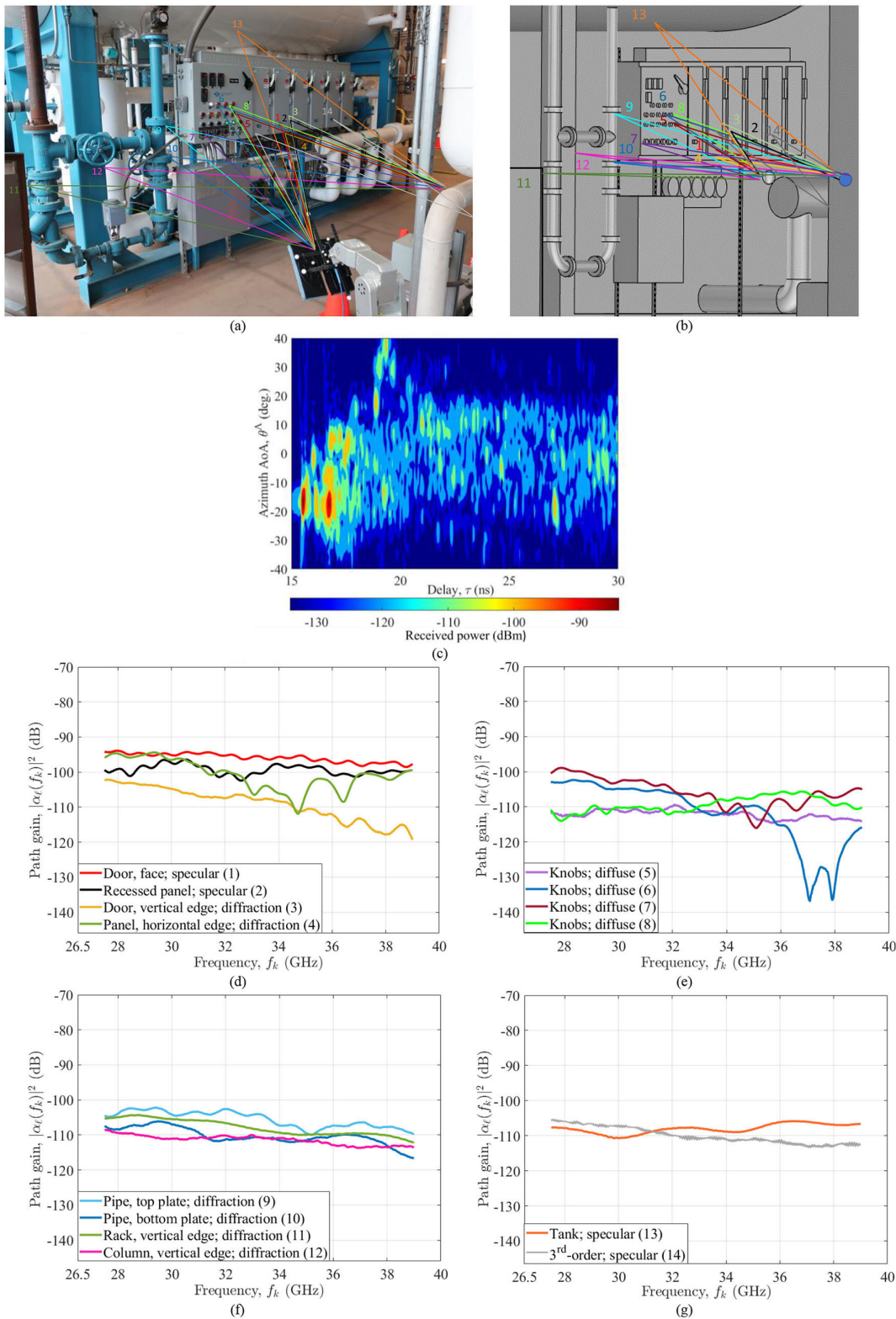
FIGURE 6. CUP measurement. (a) Photograph of the setup, with T and R facing a control panel. (b) CAD model of the environment. (c) Recorded angle-delay response $h(\tau, \theta)$. (d) Frequency dependence of paths from the center panel. (e) Frequency dependence of paths from the left panel. (f) Frequency dependence of other diffracted paths. (g) Frequency dependence of other specular paths.

measurement, and individually classified against the object on which it was incident. Specifically, the point of incidence was computed from the estimated delay and AoA of the

path, as described earlier, and classified against the object in the 3D CAD model of the environment on which the point fell. The CAD model rendered by the camera system with
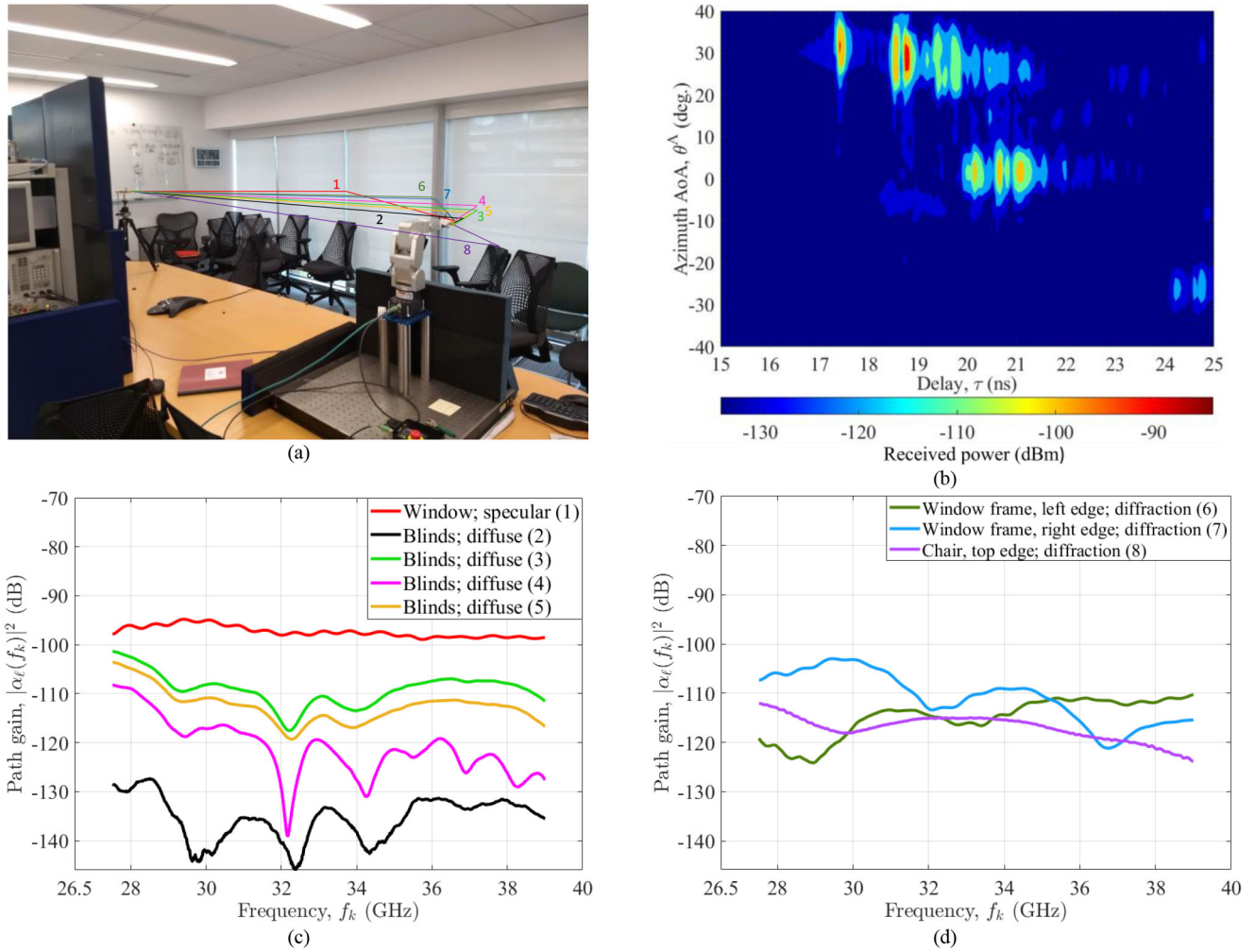
FIGURE 7. Conference room measurement with T inside. (a) Photograph of the setup, with T and R on the conference table facing the exterior window. (b) Recorded angle-delay response $h(\tau, \theta)$. (c) Frequency dependence of the paths from the exterior window. (d) Frequency dependence of the other diffracted paths.

millimeter accuracy is shown in Fig. 6(b). The 14 raytraced paths are indexed in both Fig. 6(a) and (b). In addition to classifying each path against an environment object, we also classified the incidence itself as either a specular reflection, a diffraction, or a diffuse reflection as follows:

- IF the angle of incidence (AoD) is equal to the angle of reflection (AoA): specular reflection;
- ELSE IF the point of incidence falls on a clear corner or edge in the environment: diffraction;
- ELSE: diffuse reflection.

A cluster of four paths was associated with the center panel: a specular reflection from the face of a panel door, a specular reflection from the recessed panel, a diffraction from the vertical edge of the door, and a horizontal diffraction from the bottom edge of the center panel. Their frequency dependence is shown in Fig. 6(d): not only are the specular paths stronger than the diffracted paths, their dependence is notably flatter. A cluster of four diffuse paths was associated with the left panel, covered with knobs and switches whose size is comparable to the signal wavelength. As displayed in Fig. 6(e), all four paths were weaker than the specular paths from the center panel, and most exhibited much greater variation over frequency. In fact, path 6 exhibited a peak-to-trough variation in path gain of 34.5 dB. Fig. 6(f) shows the remaining paths that were identified as diffractions: from the top and bottom plates on the pipe, the vertical edge of the rack, and the vertical edge of the column. Finally, Fig. 6(g) shows the remaining paths that were identified as specular reflections: from the cylindrical tank above the center panel and a third-order reflection.[6] Notice the distinct small-scale fluctuations of the third-order reflection.

2) CONFERENCE ROOM

A photograph of the measurement setup in the conference room appears in Fig. 7(a), where the T and R were placed on

---

6. Note that all 14 paths in the CUP, save one, were single incidence, for which the incident objects could be classified unambiguously. Rather, the third-order specular reflection was classified through visual inspection, by tracing the delay and AoA of the path in the CAD model, to find the three incident objects.

(a)

(b)

(c)
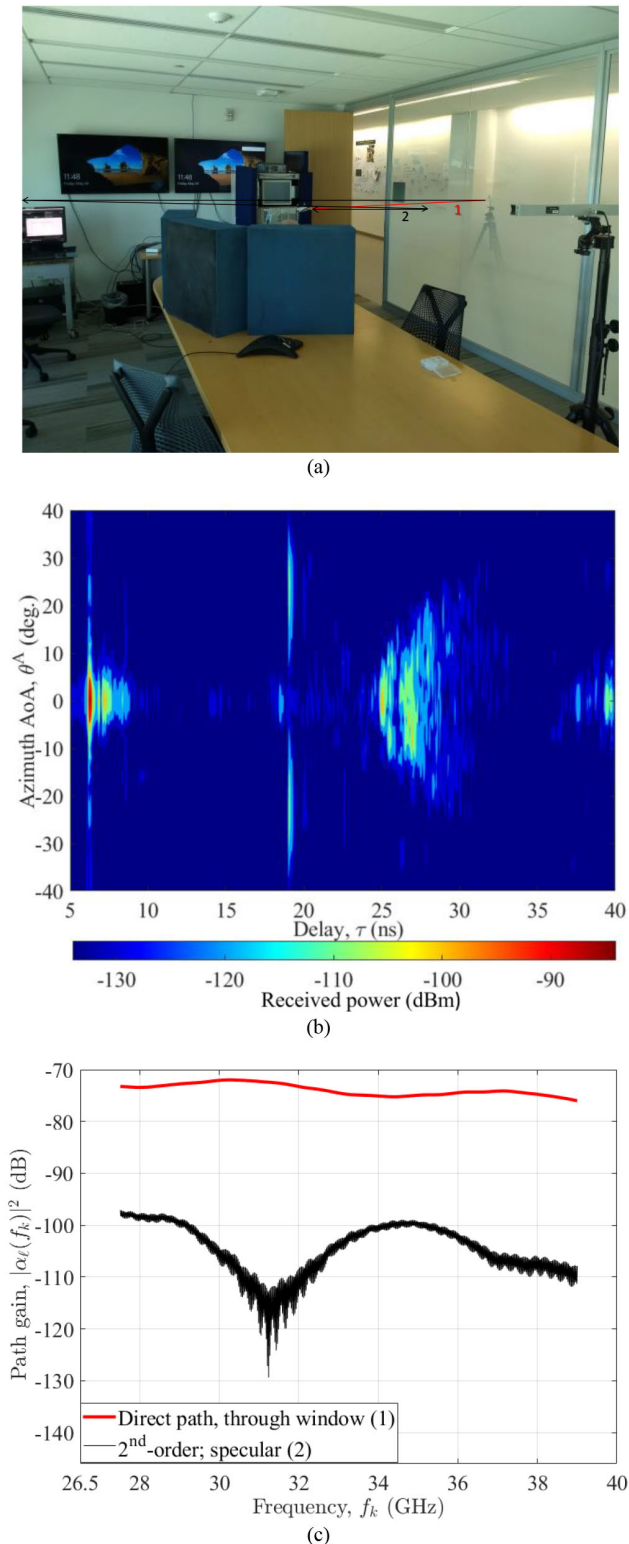
FIGURE 8. Conference room measurement with T outside. (a) Photograph of the setup, with T on a tripod outside the room and R on a conference table inside the room, facing each other. (b) Recorded angle-delay response $h(\tau, \theta)$. (c) Frequency dependence of the two paths extracted.

the conference table and pointed towards the exterior window, with the blinds closed. Also shown in the figure are the eights paths extracted from the measurement. A cluster of

five paths was associated with the exterior window, whose frequency dependencies are shown in Fig. 7(c): one strong specular reflection from the window and four weaker diffuse reflections from the blinds. As in the CUP, the specular reflections were stronger – up to 38 dB stronger – and exhibited a much flatter dependence than the diffuse reflections. And here as well, the diffuse reflections exhibited a much larger peak-to-trough variation, of up to 30.9 dB. The large fluctuations in the diffuse path may in fact stem from the combination of multiple diffuse paths originating from the densely packed blinds – beyond the resolution capability of the system – that appear as a single path, generating deep nulls at certain frequencies. The remainder of the paths are shown in Fig. 7(d), attributed to diffractions: from the left and right edges of the metal frame separating the window panes – they exhibit very similar behavior – and from the top edge of a chair.

Another measurement was taken in the conference room, however with the T antenna outside, as shown in Fig. 8(a). Only two paths were extracted since any detected path had to penetrate the double-paned interior window of the conference room (most likely refracted): the direct path to R and a second-order reflection from the exterior window to the interior window and back to R. Consistent with the higher-order reflection in the CUP, many small-scale fluctuations were observed.

The frequency dependence of all of the paths in the CUP and the conference room were quantified and reported in Table 4 as follows: the mean path gain over the band, the slope of a line fit (in least squares sense) to the path gain over the band and the resultant standard deviation of the residual, and the peak-to-trough path gain. Also reported in the table are the geometrical properties of the paths used for classification. Overall, it can be observed from the mean path gain that the specular paths are the strongest, followed by the diffracted paths, and then by the diffuse paths. Not only are the specular paths the strongest, they are also the least variant across frequency – as indicated both by the peak-to-trough deviation and the standard deviation of the residual – followed by the diffracted and diffuse paths in the same order. Out of the 24 total paths reported, all but four exhibited a negative slope – as low as -0.13 dB/GHz for a specular path to as high as -2.27 dB/ GHz for a diffuse path – and the four with positive slope were mostly mild, indicating that greater path loss is indeed expected at higher frequencies.

V. CONCLUSION

This paper proposes a novel methodology to measure the frequency dependence of channel paths across the mmWave spectrum. The methodology emphasizes calibration of the measurement equipment so that the results reported represent the channel alone (and not the channel coupled with the channel sounder), departing from methodologies employed by other organizations reporting on this topic in the past, with conflicting results. In the process, we proposed an extension

TABLE 4. Estimated properties of the paths extracted from the two real environments.

Path	Frequency-Dependent Path Gain			Geometrical Properties		
	Mean (dB)	Slope / Std (dB/GHz) / (dB)	Peak-to-Trough (dB)	delay (ns)	AoA AZ / EL (deg)	AoD AZ / EL (deg)
Central Utility Plant						
Door, face; specular (1)	-95.9	-0.34 / 0.006	4.6	15.4	-16.7 / -1.3	5.5 / 7.6
Recessed panel; specular (2)	-99.4	-0.13 / 0.025	6.0	16.7	-18.3 / 0.8	-3.3 / 9.7
Door, vertical edge; diffraction (3)	-109.0	-1.35 / 0.027	17.1	15.4	-17.6 / -5.1	5.0 / 4.4
Panel, horizontal edge (4)	-100.8	-0.83 / 0.015	17.6	16.7	-17.1 / 4.1	-2.0 / 12.6
Knobs, diffuse (5)	-112.1	-0.22 / 0.030	5.2	15.9	-1.9 / -2.2	12.9 / 6.5
Knobs, diffuse (6)	-111.7	-2.27 / 0.122	34.5	15.9	-9.1 / 8.0	9.8 / 13.5
Knobs, diffuse (7)	-105.8	-0.84 / 0.020	17.1	16.8	-14.3 / 5.9	0.3 / 13.6
Knobs, diffuse (8)	-109.4	0.47 / 0.007	8.4	15.8	-12.6 / 7.6	7.6 / 13.9
Pipe, top plate; diffraction (9)	-105.5	-0.58 / 0.069	7.8	16.7	4.1 / 2.6	12.8 / 9.0
Pipe, bottom plate; diffraction (10)	-110.3	-0.55 / 0.020	10.5	16.7	4.6 / -4.8	13.2 / 5.0
Rack, vertical edge; diffraction (11)	-107.8	-0.64 / 0.032	7.9	19.2	38.3 / -3.0	21.5 / 6.0
Column, vertical edge; diffraction (12)	-111.4	-0.36 / 0.022	5.1	18.8	17.5 / -2.3	12.9 / 6.3
Tank; specular (13)	-108.0	0.28 / 0.058	4.9	21.5	-13.0 / 31.0	-6.4 / 37.5
3rd-order; specular (14)	-110.0	-0.67 / 0.026	8.2	27.0	-18.3 / -0.9	5.0 / 0.0
Conference Room (Transmitter inside)						
Window; specular (1)	-97.3	-0.29 / 0.057	4.1	17.5	28.7 / 3.6	-9.3 / 3.6
Blinds; diffuse (2)	-135.4	0.12 / 0.222	18.6	20.5	-1.2 / -1.8	-10.0 / -1.2
Blinds; diffuse (3)	-109.1	-0.20 / 0.194	16.2	20.6	1.6 / 1.9	-7.9 / 1.3
Blinds; diffuse (4)	-121.1	-1.20 / 0.177	30.9	20.6	1.6 / 5.8	-8.0 / 4.0
Blinds; diffuse (5)	-112.5	-0.46 / 0.185	15.7	20.6	1.2 / 0.7	-8.2 / 0.5
Window frame, left edge; diffraction (6)	-114.9	1.01 / 0.041	13.9	18.7	29.1 / -1.5	-9.7 / -1.5
Window frame, right edge; diffraction (7)	-110.7	-1.34 / 0.125	18.2	18.7	28.0 / -0.3	- 8.7 / -0.3
Chair, top edge; diffraction (8)	-117.1	-0.59 / 0.047	11.7	14.9	8.4 /-16.1	-21.0 / -8.5
Conference Room (Transmitter outside)						
Direct path, through window (1)	-73.8	-0.26 / 0.024	4.0	6.3	0.0 / 8.1	0.0 / 8.0
2nd-order; specular (2)	-104.7	-0.32 / 0.137	32.3	38.3	-0.1 / 8.8	0.0 / 9.0

of the SAGE super-resolution to extract the frequency dependence of individual channel paths. Our findings confirm that the line-of-sight path is indeed frequency invariant – a well understood result in theory – but reported nowhere else to date at mmWave to our knowledge. More interestingly, we found that pathloss increases across frequency, but that the rate depends heavily on the type of path. Namely, specular paths – the strongest after the line-of-sight path and thus critical for maintaining connectivity when the line-of-sight path is blocked – varied only between 0.13 – 0.34 dB/GHz, whereas the weaker diffracted and diffuse paths varied up to 2.27 dB/GHz. In particular, the diffuse paths exhibited the deepest fades, up to almost 35 dB from peak to trough.

REFERENCES

[1] H. T. Friis, "A note on a simple transmission formula," *Proc. IRE*, vol. 34, no. 5, pp. 254–256, May 1946.
[2] Z. Pi and F. Khan, "An introduction to millimeter-wave mobile broadband systems," *IEEE Commun. Mag.*, vol. 49, no. 6, pp. 101–107, Jun. 2011.
[3] S. Salous *et al.*, "Millimeter-wave propagation: Characterization and modeling toward fifth-generation systems. [Wireless Corner]," *IEEE Antennas Propag. Mag.*, vol. 58, no. 6, pp. 115–127, Dec. 2016.
[4] O. H. Koymen, A. Partyka, S. Subramanian, and J. Li, "Indoor mm-Wave channel measurements: Comparative study of 2.9 GHz and 29 GHz," in *Proc. IEEE Global Commun. Conf. (GLOBECOM)*, 2015, pp. 1–6.

[5] V. Raghavan *et al.*, "Millimeter-wave MIMO prototype: Measurements and experimental results," *IEEE Commun. Mag.*, vol. 56, no. 1, pp. 202–209, Jan. 2018.
[6] G. R. Maccartney, T. S. Rappaport, S. Sun, and S. Deng, "Indoor office wideband millimeter-wave propagation measurements and channel models at 28 and 73 GHz for ultra-dense 5G wireless networks," *IEEE Access*, vol. 3, pp. 2388–2424, 2015.
[7] Y. Xing and T. S. Rappaport, "Propagation measurement system and approach at 140 GHz-moving to 6G and above 100 GHz," in *Proc. IEEE Global Commun. Conf. (GLOBECOM)*, 2018, pp. 1–6.
[8] C.-L. Cheng, S. Kim, and A. Zajić, "Comparison of path loss models for indoor 30 GHz, 140 GHz, and 300 GHz channels," in *Proc. 11th Eur. Conf. Antennas Propagat. (EUCAP)*, 2017, pp. 716–720.
[9] P. Zhang, J. Li, H. Wang, and H. Wang, "Indoor small-scale spatiotemporal propagation characteristics at multiple millimeter-wave bands," *IEEE Antennas Wireless Propag. Lett.*, vol. 17, no. 12, pp. 2250–2254, Dec. 2018.
[10] Y. Zhou *et al.*, "Multi-frequency millimeter-wave large-scale path loss characterization for indoor environment," in *Proc. Int. Symp. Antennas Propagat. (ISAP)*, 2019, pp. 1–3.
[11] D. Dupleich *et al.*, "Multi-band indoor propagation characterization by measurements from 6 to 60 GHz," in *Proc. 13th Eur. Conf. Antennas Propagat. (EuCAP)*, 2019, pp. 1–5.
[12] M. Khalily, S. Taheri, S. Payami, M. Ghoraishi, and R. Tafazolli, "Indoor wideband directional millimeter wave channel measurements and analysis at 26 GHz, 32 GHz, and 39 GHz," *Trans. Emerg. Telecommun. Technol.*, vol. 29, no. 10, 2018, Art. no. e3311.
[13] A. Bamba, F. Mani, and R. D'Errico, "Millimeter-wave indoor channel characteristics in V and E bands," *IEEE Trans. Antennas Propag.*, vol. 66, no. 10, pp. 5409–5424, Oct. 2018.

[14] S. Salous *et al.*, "Radio propagation measurements and modeling for standardization of the site general path loss model in International Telecommunications Union recommendations for 5G wireless networks," *Radio Sci.*, vol. 55, no. 1, pp. 1–12, Jan. 2020.

[15] S. Salous, A. Al-Jzari, M. Abdulali, and J. Towers, "Multi-band measurements in indoor environments," in *Proc. 15th Eur. Conf. Antennas Propagat. (EuCAP)*, 2021, pp. 1–4.

[16] Y. L. C. D. Jong, J. A. Pugh, M. Bennai, and P. Bouchard, "2.4 to 61 GHz multiband double-directional propagation measurements in indoor office environments," *IEEE Trans. Antennas Propag.*, vol. 66, no. 9, pp. 4806–4820, Sep. 2018.

[17] M. H. C. Dias and G. L. Siqueira, "Indoor 1.8 GHz AOA-TDOA measurements extending the use of a wideband propagation channel sounder with the synthetic aperture concept," in *Proc. Eur. Microw. Conf.*, vol. 2, 2005, pp. 1191–1194.

[18] S. Ranvier, M. Kyro, K. Haneda, T. Mustonen, C. Icheln, and P. Vainikainen, "VNA-based wideband 60 GHz MIMO channel sounder with 3-D arrays," in *Proc. IEEE Radio Wireless Symp.*, 2009, pp. 308–311.

[19] C. Gentile, S. M. Lopez, and A. Kik, "A comprehensive spatial-temporal channel propagation model for the ultrawideband spectrum 2–8 GHz," *IEEE Trans. Antennas Propag.*, vol. 58, no. 6, pp. 2069–2077, Jun. 2010.

[20] A. Mannesson, B. Bernhardsson, M. A. Yaqoob, and F. Tufvesson, "Optimal virtual array length under position imperfections," in *Proc. IEEE 8th Sensor Array Multichannel Signal Process. Workshop (SAM)*, 2014, pp. 5–8.

[21] B. Chen, Z. Zhong, B. Ai, and D. G. Michelson, "Moving virtual array measurement scheme in high-speed railway," *IEEE Antennas Wireless Propag. Lett.*, vol. 15, pp. 706–709, 2015.

[22] H. Hayashi and T. Ohtsuki, "DOA estimation in MIMO radar using temporal spatial virtual array with MUSIC algorithm," in *Proc. 9th Int. Conf. Signal Process. Commun. Syst. (ICSPCS)*, 2015, pp. 1–6.

[23] H.-A. Nguyen, K. Mahler, M. Peter, W. Keusgen, T. Eichler, and H. Mellein, "Estimation of DoA based on large-scale virtual array data," in *Proc. 10th Eur. Conf. Antennas Propagat. (EuCAP)*, 2016, pp. 1–4.

[24] H.-A. Nguyen, W. Keusgen, and T. Eichler, "Instantaneous direction of arrival measurements in mobile radio channels using virtual circular array antennas," in *Proc. IEEE Globecom Workshops (GC Wkshps)*, 2016, pp. 1–7.

[25] T. Zhou, C. Tao, S. Salous, and L. Liu, "Measurements and analysis of angular characteristics and spatial correlation for high-speed railway channels," *IEEE Trans. Intell. Transp. Syst.*, vol. 19, no. 2, pp. 357–367, Feb. 2018.

[26] A. W. Mbugua, W. Fan, Y. Ji, and G. F. Pedersen, "Millimeter wave multi-user performance evaluation based on measured channels with virtual antenna array channel sounder," *IEEE Access*, vol. 6, pp. 12318–12326, 2018.

[27] H. Qiao, P. Sarangi, Y. Alnumay, and P. Pal, "Sample complexity trade-offs for synthetic aperture based high-resolution estimation and detection," in *Proc. IEEE 11th Sensor Array Multichannel Signal Process. Workshop (SAM)*, 2020, pp. 1–5.

[28] D. Caudill, P. B. Papazian, C. Gentile, J. Chuang, and N. Golmie, "Omnidirectional channel sounder with phased-arrayAntennas for 5G mobile communications," *IEEE Trans. Microw. Theory Techn.*, vol. 67, no. 7, pp. 2936–2945, Jul. 2019.

[29] D. Caudill, J. Chuang, S. Y. Jun, C. Gentile, and N. Golmie, "Real-time mmWave channel sounding through switched beamforming with 3-D dual-polarized phased-array antennas," *IEEE Trans. Microw. Theory Techn.*, vol. 69, no. 11, pp. 5021–5032, Nov. 2021.

[30] J. A. Högbom, "Aperture synthesis with a non-regular distribution of interferometer baselines," *Astronomy Astrophys. Supplement Series*, vol. 15, pp. 417–426, Jun. 1974.

[31] J. A. Fessler and A. O. Hero, "Space-alternating generalized expectation-maximization algorithm," *IEEE Trans. Signal Process.*, vol. 42, no. 10, pp. 2664–2677, Oct. 1994.

[32] A. Richter, *Estimation of Radio Channel Parameters: Models and Algorithms*. Blacksburg, VA, USA: ISLE, 2005.

[33] R. Schmidt, "Multiple emitter location and signal parameter estimation," *IEEE Trans. Antennas Propag.*, vol. 34, no. 3, pp. 276–280, Mar. 1986.

[34] R. Roy and T. Kailath, "ESPRIT-estimation of signal parameters via rotational invariance techniques," *IEEE Trans. Acoust. Speech Signal Process.*, vol. 37, no. 7, pp. 984–995, Jul. 1989.

[35] A. J. Weiss *et al.*, "Large-signal network analysis for over-the-air test of up-converting and down-converting phased arrays," in *Proc. IEEE MTT-S Int. Microw. Symp. (IMS)*, 2019, pp. 622–625.

[36] A. J. Weiss *et al.*, "Configuration and control of a millimeter-wave synthetic aperture measurement system with uncertainties," in *Proc. 95th ARFTG Microw. Meas. Conf. (ARFTG)*, 2020, pp. 1–4.

[37] L. J. Foged, F. Saccardi, F. Mioc, and P. O. Iversen, "Spherical near field offset measurements using downsampled acquisition and advanced NF/FF transformation algorithm," in *Proc. 10th Eur. Conf. Antennas Propagat. (EuCAP)*, 2016, pp. 1–3.

[38] N. R. Leonor, R. F. S. Caldeirinha, and M. G. Sánchez, and T. R. Fernandes, "A three-dimensional directive antenna pattern interpolation method," *IEEE Antennas Wireless Propag. Lett.*, vol. 15, pp. 881–884, 2015.

[39] A. Weiss, *Characterization of a Vector Network Analyzer Based Millimeter-Wave Channel Sounder*. Golden, CO, USA: Colorado School Mines, 2018.

[40] D. K. Cheng, *Fundamentals of Engineering Electromagnetics*. Hoboken, NJ, USA: Prentice Hill, 1993.

[41] T. S. Rappaport *et al.*, "Millimeter wave mobile communications for 5G cellular: It will work!," *IEEE Access*, vol. 1, pp. 335–349, 2013.

[42] J. Kaiser and R. Schafer, "On the use of the I0-sinh window for spectrum analysis," *IEEE Trans. Acoust. Speech Signal Process.*, vol. 28, no. 1, pp. 105–107, Feb. 1980.

[43] A. F. Molisch, *Wireless Communications*. Vol. 34. Hoboken, NJ, USA: Wiley, 2012.

[44] A. J. Van Den Biggelaar, A. B. Smolders, U. Johannsen, B. F. Jamroz, and D. F. Williams, "Correction of the measured phase Of the radiation pattern Of millimeter-wave antennas," in *Proc. Antenna Meas. Techn. Assoc. Symp. (AMTA)*, 2020, pp. 1–5.

[45] W. G. Newhall and J. H. Reed, "A geometric air-to-ground radio channel model," in *Proc. MILCOM*, vol. 1, 2002, pp. 632–636.

DAMLA GUVEN (Member, IEEE) received the B.E. degree in electronics and computer systems engineering from the Victoria University of Wellington, New Zealand, in 2014, and the M.E. degree in electrical and electronics engineering from the University of Auckland, New Zealand, in 2019. In 2014, she joined Spark New Zealand as a Radio Frequency Engineer. Since 2019, she has been a Researcher with Communications Technology Laboratory, National Institute of Standards and Technology. Her current research interests include signal processing for wireless communications, channel modeling, and characterization of millimeter wave frequencies.

BENJAMIN F. JAMROZ received the Ph.D. degree in applied mathematics from the University of Colorado, Boulder, CO, USA, in 2009, where he developed new analytical and numerical models for plasma physics. His work since has focused on modeling physical phenomena, such as electromagnetics, as well as applying machine learning techniques to complex analytics. In 2017, he joined the Communications Technology Laboratory with the National Institute of Standards and Technology, where he models and analyzes the complex systems required for high-frequency communications.

JACK CHUANG received the Ph.D. degree from The Pennsylvania State University in 2008, where he was a Graduate Research Assistant with Communications and Space Sciences Laboratory. He then worked with BAE Systems in electronic warfare and Cisco Systems in spectrum sharing. He is currently with Communication Technology Lab, NIST, Gaithersburg, USA, developing 5G mmWave channel sounders.
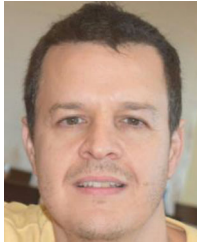
CAMILLO GENTILE (Member, IEEE) received the Ph.D. degree in electrical engineering from The Pennsylvania State University in 2001. He joined the National Institute of Standards and Technology, Gaithersburg, MD, USA, in 2001, where he is currently leading the Radio Access and Propagation Metrology Group and the NextG Channel Measurement and Modeling Project in the Communications Technology Laboratory. He has authored over 90 peer-reviewed journal and conference papers, a book on geolocation techniques and a book on millimeter-wave and sub-terahertz channel propagation modeling. His current interests include channel modeling and physical-layer modeling for 5G and 6G wireless systems.

ROBERT D. HORANSKY (Member, IEEE) received the B.A. degree in chemistry and the Ph.D. degree in physics from the University of Colorado, Boulder, CO, USA, in 1999 and 2005, respectively. His thesis work focused on low-noise dielectric measurements on novel materials in molecular electronics. Since 2005, he has been with the National Institute of Standards and Technology, Boulder, CO, USA, where he started out developing the highest resolving power energy dispersive sensor to date. He then went on to develop metrology techniques for single photon sensors in nuclear radiation and optical power measurements. In 2015, he joined the Metrology for Wireless Systems Project in the Communications Technology Laboratory, NIST developing calibrations and traceability for millimeter-wave wireless systems and reverberation-chamber measurements for cellular applications. He is the Secretary of the IEEE P1765 Standards Working Group on Uncertainty for EVM.

KATE A. REMLEY (Fellow, IEEE) was born in Ann Arbor, MI, USA. She received the Ph.D. degree in electrical and computer engineering from Oregon State University, Corvallis, in 1999. From 1983 to 1992, she was a Broadcast Engineer in Eugene, OR, USA, and serving as a Chief Engineer of an AM/FM Broadcast Station from 1989 to 1991. In 1999, she joined the RF Technology Division of the National Institute of Standards and Technology (NIST), Boulder, CO, USA, as an Electronics Engineer. She is currently the Leader of the Metrology for Wireless Systems Project with NIST, where her research activities include development of calibrated measurements for microwave and millimeter-wave wireless systems and standardized over-the-air test methods for the wireless industry. She was a recipient of the Department of Commerce Bronze and Silver Medals, the ARFTG Best Paper Award, and the NIST Schlichter Award. He is a member of the Oregon State University Academy of Distinguished Engineers. She was the Chair of the MTT-11 Technical Committee on Microwave Measurements from 2008 to 2010, the Editor-in-Chief of *IEEE Microwave Magazine* from 2009 to 2011, and the Chair of the MTT Fellow Evaluating Committee from 2017 to 2018. She was a Distinguished Lecturer for the IEEE Electromagnetic Compatibility Society from 2016 to 2017 and is the Co-Technical Program Chair for the IEEE International Microwave Symposium IMS2022.

DYLAN F. WILLIAMS (Life Fellow, IEEE) received the Ph.D. degree in electrical engineering from the University of California at Berkeley, Berkeley, in 1986. He joined the Electromagnetic Fields Division with the National Institute of Standards and Technology in 1989, where he develops electrical waveform and microwave metrology. He has published over 140 technical papers. He is the recipient of the Department of Commerce Bronze and Silver Medals, the Astin Measurement Science Award, two Electrical Engineering Laboratory's Outstanding Paper Awards, three Automatic RF Techniques Group (ARFTG) Best Paper Awards, the ARFTG Automated Measurements Technology Award, the IEEE Morris E. Leeds Award, the European Microwave Prize, and the 2013 IEEE Joseph F. Keithley Award. He also served as an Editor for the IEEE TRANSACTIONS ON MICROWAVE THEORY AND TECHNIQUES from 2006 to 2010, an Executive Editor for the IEEE TRANSACTIONS ON TERAHERTZ SCIENCE AND TECHNOLOGY, and the 2017 President of the IEEE Microwave Theory and Techniques Society.

JEANNE T. QUIMBY (Senior Member, IEEE) received the B.S. degree from the University of California at San Diego in 1998 and the M.S. and Ph.D. degrees from The Ohio State University in 2001 and 2005, respectively. In 2006, she joined the Space and Naval Warfare Systems Center Pacific (currently known as the NIWC-Pacific) as a Communication Expert and Researcher. Since 2015, she has been working with the National Institute of Standards and Technology in the Communication Technology Laboratory. Her current research focuses on the metrology of channel sounding, propagation in manufacturing facilities, and physical layer measurements on telecommunication devices' performances. She has developed a flexible, portable millimeter-wave measurement system to support the design and repeatable laboratory testing of 5G wireless communications devices. She has also launched enhanced channel sounder verification through the formation of the IEEE standard 2982 working group. She was the recipient of the Department of Commerce Bronze Award in 2019 for recognition for developing innovative measurement methods, a state-of-the-art testbed, and extensive first-in-class measurement data sets that led to a Comprehensive Guide to Industrial Wireless Systems Deployments. She is the current Commission A chair for the United States National Committee for Union Radio Scientifique Internationale (USNC URSI). Since 2021, she has been serving as the current Secretary for the USNC URSI Women in Radio Science Chapter.

ALEC J. WEISS (Member, IEEE) received the B.S. degree in electrical and computer engineering from the University of Colorado at Boulder, Boulder, CO, USA, in 2017, and the M.S. degree in electrical engineering from the Colorado School of Mines, Golden, CO, USA, in 2018. He is currently pursuing the Ph.D. degree in electrical engineering in a joint collaboration with NIST and Colorado School of Mines. His research interests include millimeter-wave measurements, 5G communications systems, and high-performance computing for electromagnetic applications.

RODNEY LEONHARDT received the B.S. degree in physics and the M.S. degree in electrical engineering. He has been a Member of the Optoelectronics Division and the Quantum Electronics and Photonics Division, NIST, where he is currently a Staff Member of the RF Technology Division.